

**Realization of ideal unconventional Weyl states with arbitrary topological charge**Yuanchuan Biao  and Rui Yu \**School of Physics and Technology, Wuhan University, Wuhan 430072, China  
and Wuhan Institute of Quantum Technology, Wuhan 430206, China* (Received 21 June 2022; revised 1 August 2023; accepted 25 September 2023; published 17 October 2023)

Weyl points in crystalline materials can be treated as magnetic monopoles in momentum space, with topological charges inscribed by Chern numbers. The main method of finding Weyl states with topological charges greater than one, i.e., unconventional Weyl states, is to take advantage of crystal symmetries, but the maximum topological charge that can be achieved is four. Here we provide a unified scheme for realizing a pair of Weyl points using long-range spin-orbit coupling. This scheme requires no additional symmetry other than the translational symmetry of the crystal and allows the realization of the Weyl point with arbitrary topological charges. We give a concrete method for its realization in a circuit system and verify it experimentally. This discovery reveals a scheme for realizing ideal unconventional Weyl states and using long-range spin-orbit coupling for exotic states.

DOI: [10.1103/PhysRevB.108.165128](https://doi.org/10.1103/PhysRevB.108.165128)**I. INTRODUCTION**

Weyl semimetals have been extensively investigated in quantum and classical systems in recent decades for their ability to support Weyl points [1–15]. In crystals, the Weyl points with distinct chiralities, either left-handed or right-handed, can be regarded as monopoles and antimonopoles in momentum space. According to the no-go theorem, Weyl points with opposite chirality always appear in pairs in periodic lattice systems [16]. Thus, the simplest and most fundamental case is a material with only two Weyl points, known as the ideal Weyl material. The two Weyl points in the ideal Weyl material cannot be trivially gapped out and possess physics that may not be favored for multipair Weyl points [17–20]. However, most of the previously investigated Weyl materials are based exclusively on inversion symmetry broken systems, where the number of Weyl pairs is at least two. Realizing the ideal Weyl states must break the time-reversal symmetry, which is a significant challenge in the experiment. Although magnetic Weyl semimetals have been reported [21–24], the experimentally confirmed ideal Weyl materials remain scarce [25–27].

On the other hand, the monopole charge of a Weyl point can be greater than one. Such a Weyl point lacks a high-energy counterpart known as the unconventional Weyl point. In recent years, considerable efforts have been made to investigate the unconventional Weyl points [28–42]. These efforts are mainly accomplished in the following two ways. The first is to design multifold degenerate linear band crossing points with multiple bands. The second is to design nonlinear band crossing points with two energy bands. Both methods are based on symmetries, such as time-reversal symmetry, crystalline rotational symmetry, etc., to achieve the unconventional Weyl points. Symmetry facilitates the design of the unconventional

Weyl states in crystalline materials, but it also has limitations. For instance, the crystals contain only two-, three-, four- and sixfold rotational symmetry, limiting the topological charge of the Weyl point typically to two, three, or four [35,39]. Even if more complex symmetries, such as the glide plane or the screw axis in the nonsymmorphic space group, are included, the topological charge is still limited to a few values. In addition, an essential reason for the widespread interest in the Weyl state is that it requires only the translational symmetry of the crystal and does not require the protection of any additional symmetry. Thus, it presents strong topological stability, and the only way to eliminate the Weyl points is to annihilate two antichirality Weyl points together. Based on the above discussions, two questions naturally arise: Is it possible to design the unconventional Weyl points not induced by crystal symmetry? Can the topological charge of the Weyl point can be equal to an arbitrary integer value, not just a few currently available values.

**II. MODEL HAMILTONIAN**

This paper provides a scheme for implementing the ideal Weyl states with an arbitrary topological charge by long-range spin-orbit coupling instead of symmetries. Our scheme is based on the following two-band model Hamiltonian:

$$H = \mathbf{h}(\mathbf{k}) \cdot \boldsymbol{\sigma}, \quad (1)$$

where  $\boldsymbol{\sigma} = (\sigma_x, \sigma_y, \sigma_z)$  are the Pauli matrices and  $\mathbf{h}(\mathbf{k}) = (h_1(\mathbf{k}), h_2(\mathbf{k}), h_3(\mathbf{k}))$ . We take

$$h_1(\mathbf{k}) - ih_2(\mathbf{k}) = (\alpha \cos k_x - i\beta \cos k_y)^N \quad (2)$$

and

$$h_3(\mathbf{k}) = m_0 + \gamma_1 \sin k_x + \gamma_2 \sin k_y + \gamma_3 \sin k_z, \quad (3)$$

where  $\alpha$ ,  $\beta$ ,  $\gamma_{1,2,3}$ , and  $m_0$  are real parameters and  $N$  is an arbitrary positive integer. For this two-band model, the

\*yurui@whu.edu.cn

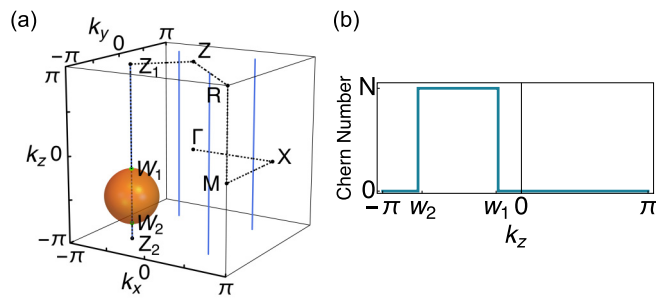


FIG. 1. Topological properties of the model Hamiltonian Eq. (1). (a) The geometric picture for the pair of Weyl points generated by Hamiltonian Eq. (1) and the high-symmetry points in the three-dimensional Brillouin zone. The four blue lines are the solutions of  $h_1(\mathbf{k}) = h_2(\mathbf{k}) = 0$ . The orange closed surface is the solutions of  $h_3(\mathbf{k}) = 0$ . Their intersection points  $W_1$  and  $W_2$  are the gap closing points of the Hamiltonian Eq. (1), namely, the Weyl points. (b) The Chern number as a function of  $k_z$ . At the Weyl point, the change of the topological Chern number is equal to the topological charge of the Weyl point.

energy bands cross and form the Weyl points at the  $\mathbf{k}$  points where  $h_1(\mathbf{k})$ ,  $h_2(\mathbf{k})$ , and  $h_3(\mathbf{k})$  vanish. The number of Weyl points can be tuned by the coefficients in Eqs. (2) and (3). It is easy to check that the solutions for  $h_1(\mathbf{k}) = h_2(\mathbf{k}) = 0$  form four straight lines in the three-dimensional Brillouin zone, which are located at  $(k_x, k_y) = (\pm\pi/2, \pm\pi/2)$  points and along the  $k_z$  direction. Solutions for  $h_3(\mathbf{k}) = 0$  may form a closed surface as shown in Fig. 1(a) in orange. By selecting the appropriate parameters, the orange surface may intersect with one of the four straight lines, for example, the line located at  $(k_x, k_y) = (-\pi/2, -\pi/2)$ , and obtain two intersection points  $W_1$  and  $W_2$  as shown in Fig. 1(a). These two points are the band-crossing points of Hamiltonian Eq. (1), namely, the Weyl points we are searching for.

To clarify the topological nature of the Weyl points, we expand Hamiltonian Eq. (1) at point  $(k_x, k_y) = (-\pi/2, -\pi/2)$  up to the lowest order in  $\mathbf{k}$  to obtain an effective Hamiltonian  $H_W = k^N \sigma_+ + k^N \sigma_- + m \sigma_z$ , where  $k_{\pm} = \alpha k_x \pm i \beta k_y$ ,  $\sigma_{\pm} = (\sigma_x \pm i \sigma_y)/2$  and  $m = m_0 - \gamma_1 - \gamma_2 + \gamma_3 \sin k_z$  is the mass term. The Weyl points have linear band splitting along the  $k_z$  direction and  $k^N$  band splitting along the  $k_x$  and  $k_y$  directions. Taking  $k_z$  as the parameter, the Chern number in the  $k_x$ - $k_y$  plane is calculated as  $C(k_z) = \text{sgn}(m)N/2$ , which changes by  $\pm N$  when it passes the Weyl points  $W_1$  and  $W_2$  where the mass term changes signs. Therefore, the topological charge of the Weyl point is  $\pm N$ . The above analysis confirms that a single pair of Weyl points with topological charge  $\pm N$  can be performed by Hamiltonian Eq. (1) and that the existence of Weyl points is not due to symmetry but the long-range spin-orbit coupling. Since the Hamiltonian Eq. (1) is capable of realizing a Weyl point with topological charge  $N$  equals 5, 7, or 9, whereas there is no five-, seven- or ninefold crystalline rotational symmetry or other symmetries that can protect such a Weyl point.

The model Hamiltonian Eq. (1) can implement both conventional and unconventional Weyl states with a minimum number of two bands but at the price of requiring the  $N$ th nearest-neighbor hopping terms in the form of Pauli matrices.

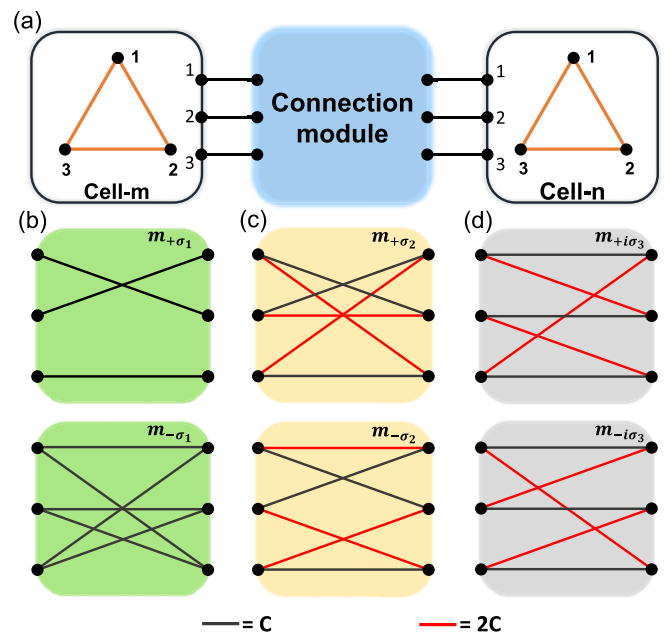


FIG. 2. Building blocks for spin-orbit coupling in circuit. (a) Schematic diagram of cells  $m$  and  $n$ , and the connection module consists of resistors, inductors and capacitors. In cells  $m$  and  $n$ , the inductors or capacitors are connected head to tail to form a loop structure with  $C_3$  symmetry that generates a twofold degenerate pseudospin space. The connection module is used to connect the nodes in cells  $m$  and  $n$ . (b)–(d) The list of designed connection modules  $m_{\pm\sigma_{x,y}}$  and  $m_{\pm i\sigma_z}$  that give  $\pm\sigma_{x,y}$  and  $\pm i\sigma_z$  types of tunneling matrices in the twofold degenerate pseudospin space. The solid lines indicate capacitors and the same color indicates devices with the same parameter.

This requirement makes it difficult to reach in condensed solid materials or artificial rigid materials. However, because of their extremely high level of connection freedom, circuit networks can be used to achieve many states of matter [43,44]. At present, the conventional Weyl states and type-II Weyl states have been discussed in circuit networks, which adopt the scheme of breaking the inversion symmetry of the system [45–48]. However, the ideal Weyl states due to broken time-reversal symmetry and unconventional Weyl states have yet to be discussed in the circuit. In the following, we present details of the realization of the ideal Weyl states with topological charge  $N$  equal to 1 and 2 in the circuit network.

### III. THE WEYL CIRCUIT WITH TOPOLOGICAL CHARGE EQUAL TO $\pm 1$

We first provide the scheme for implementing the twofold space required by Eq. (1) in the circuit and then design the hopping terms in the form of Pauli matrices in this space. The twofold space can be implemented by the pseudospin module as illustrated in Fig. 2(a). The three identical inductors are connected to a triangular structure with  $C_3$  rotational symmetry and time-reversal symmetry. These symmetries guarantee that this structure possesses an eigenstate characterized by the one-dimensional representation of the  $C_3$  symmetry group and a twofold degenerate eigenstate characterized

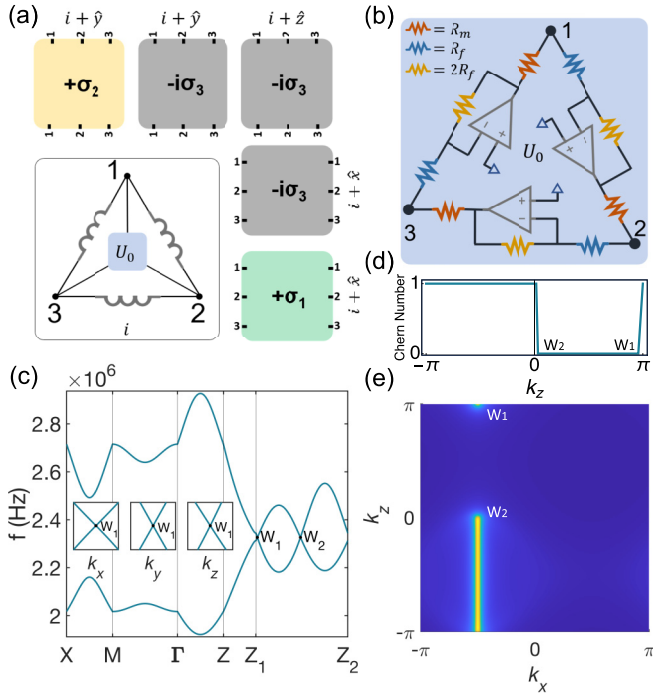


FIG. 3. The Weyl circuit with topological charge equal to  $\pm 1$ . (a) Schematic of the unit cell of Weyl circuit with  $N = 1$ . The green, gray, and yellow blocks are the connection modules used for the three-dimensional connections. Their configuration details are shown in Figs. 2(b)–2(d). The lower and left nodes in connection modules are connected to nodes 1–3 of cell  $i$ . The upper and right nodes are connected to the nodes in cell  $i + \delta$ , where  $\delta = \hat{x}, \hat{y}, \hat{z}$ . The  $U_0$  module is used to realize the on-site matrix in Eq. (4). (b) Circuit diagram of the  $U_0$  module, which consists of inverting op-amps and resistors. (c) Eigenfrequency dispersions of the Weyl circuit along high-symmetry lines, where the indices of high-symmetry points are given in Fig. 1(a). The bands cross at points  $W_1$  and  $W_2$  in the Brillouin zone. Near the crossing point, the bands are linear along the  $k_x$ ,  $k_y$ , and  $k_z$  directions. (d) The Chern number in the  $k_x$ - $k_y$  plane as a function of  $k_z$ , which changes by  $\pm 1$  when it passes by  $W_1$  and  $W_2$  points. (e) The surface states on the (010) surface. A Fermi arc links the projections of the two Weyl points on the surface Brillouin zone.

by the two-dimensional representation of the  $C_3$  symmetry group. The latter can be used as the pseudospin space requested in Eq. (1). Connecting the pseudospin modules with devices in a braided configuration allows the electrical signals to flip spins and are subject to a spin-orbit couplinglike effect as they pass between them. We design six connection modules that are proportional to  $\pm\sigma_{x,y}$  and  $\pm i\sigma_z$  matrices as depicted in Figs. 2(b)–2(d), which can be used to connect the pseudospin modules at arbitrary distances to implement the hopping terms required by the model Hamiltonian Eq. (1). More details are provided in Appendix A.

For  $N = 1$ , the Hamiltonian Eq. (1) can be explored with a square lattice described by the tight-binding Hamiltonian

$$H_{N=1} = \sum_{i,j} \sum_{k=0}^3 (c_{i+\delta_k,j}^\dagger \hat{U}_k c_{i,j} + \text{H.c.}), \quad (4)$$

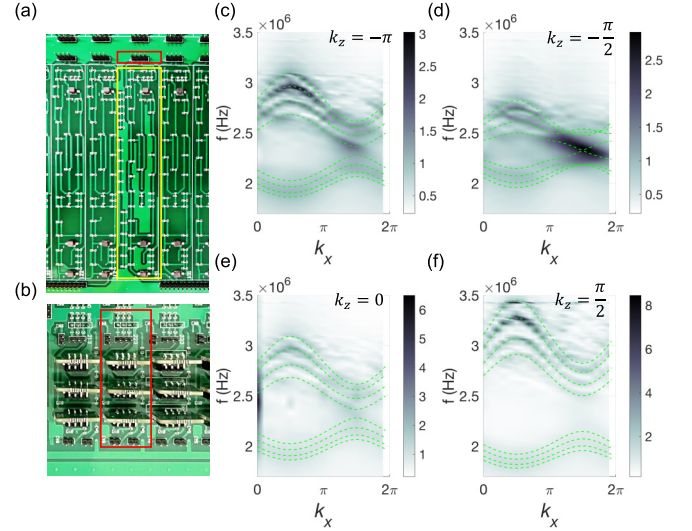


FIG. 4. The printed circuit board and the experimentally observed edge states for the  $N = 1$  Weyl circuit. (a) Unit cell of the printed circuit board fabricated according to Figs. 3(a) and 3(b). The yellow box indicates the connection modules and the inductors. The red box indicates the interface of the  $U_0$  module. (b) The printed circuit board of the  $U_0$  module. (c)–(f) The experimentally measured band structure for  $k_z = -\pi, -\pi/2, 0$ , and  $\pi/2$ . The black color represents the experimental data. The green curve is the computed band structure of a slab with four cells in the  $y$  direction. The  $k = -\pi$  and  $k = 0$  planes are close to the Weyl points, where there exists a small gap in the band structure. For the  $k = -\pi/2$  subsystem, an edge state crosses the gap. The signal source is connected to the cell at  $y = 4$ . Therefore, only the edge state localized at this boundary can be detected, while the edge state at the  $y = 1$  boundary cannot be detected. For  $k_z = \pi/2$ , there are no edge states in the gap.

where  $i$  and  $j$  indicate the lattice site,  $\delta_k$  are hopping vectors,  $\hat{U}_k$  are spin-orbit coupling operators, and their expressions are given in Table I. The hopping operators can be implemented with the connection modules illustrated in Figs. 2(b)–2(d). For example,  $\hat{U}_1$  can be constructed by connecting  $m_{\sigma_1}$  and  $m_{-i\sigma_3}$  modules in parallel and  $\hat{U}_2$  can be constructed by connecting  $m_{\sigma_2}$  and  $m_{-i\sigma_3}$  modules in parallel. The operator  $\hat{U}_0$  characterizes the coupling within the unit cell, which can be implemented by using the inverting operational amplifier as

TABLE I. The hopping vectors  $\delta_i$  and the corresponding spin-orbit coupling operators  $\hat{U}_i$  for the Weyl circuit with topological charges equal to 1 and 2.  $p \equiv (\alpha^2 - \beta^2)/2$ .  $\hat{x}, \hat{y}$ , and  $\hat{z}$  indicate the unit lattice vectors in the  $x, y$ , and  $z$  directions, respectively.

$N = 1$	$i$	0	1	2	3
	$\delta_i$	0	$\hat{x}$	$\hat{y}$	$\hat{z}$
	$\hat{U}_i$	$m_0\sigma_3$	$\frac{1}{2}\alpha\sigma_1 - \frac{i}{2}\gamma_1\sigma_3$	$\frac{1}{2}\beta\sigma_2 - \frac{i}{2}\gamma_2\sigma_3$	$-\frac{i}{2}\gamma_3\sigma_3$
	$i$	0	1	2	3
	$\delta_i$	0	$\hat{x}$	$\hat{y}$	$\hat{z}$
$N = 2$	$\hat{U}_i$	$p\sigma_1 + m_0\sigma_3$	$-\frac{i}{2}\gamma_1\sigma_3$	$-\frac{i}{2}\gamma_2\sigma_3$	$-\frac{i}{2}\gamma_3\sigma_3$
	$i$	4	5	6	7
	$\delta_i$	$2\hat{x}$	$2\hat{y}$	$\hat{x} + \hat{y}$	$\hat{x} - \hat{y}$
	$\hat{U}_i$	$\frac{\alpha^2}{4}\sigma_1$	$-\frac{\beta^2}{4}\sigma_1$	$\frac{\alpha\beta}{2}\sigma_2$	$\frac{\alpha\beta}{2}\sigma_2$

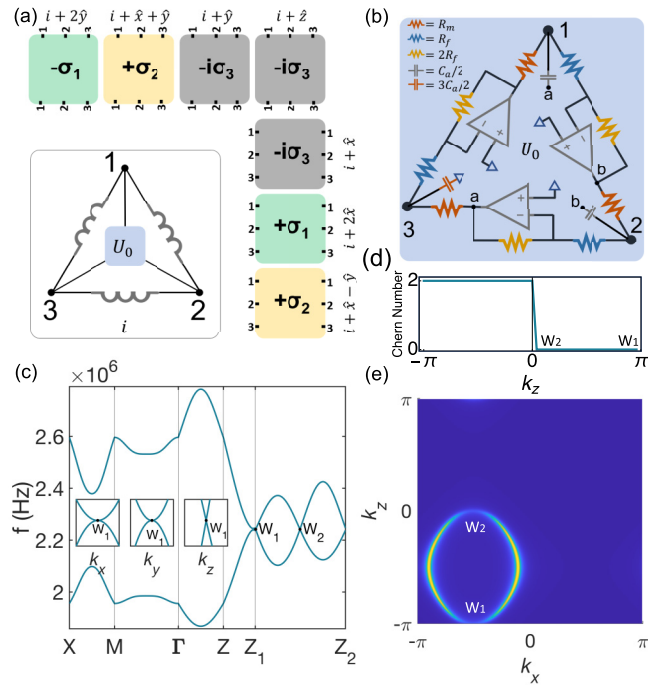


FIG. 5. The Weyl circuit with topological charge equal to  $\pm 2$ . (a) Schematic of the unit cell of Weyl circuit with  $N = 2$ . The green, gray, and yellow blocks are the connection modules used for the three-dimensional connections. Their configuration details are shown in Figs. 2(b)–2(d). The lower and left nodes in connection modules are connected to nodes 1–3 of cell  $i$ . The upper and right nodes are connected to the nodes in cell  $i + \delta$ , where  $\delta = \hat{x}, \hat{y}, \hat{z}, 2\hat{x}, 2\hat{y}, \hat{x} + \hat{y}$ , and  $\hat{x} - \hat{y}$ . The  $U_0$  module is used to realize the on-site matrix in Eq. (6). (b) Circuit diagram of the  $U_0$  module, which consists of inverting op-amps, capacitors, and resistors. (c) Eigenfrequency dispersion of the Weyl circuit along high-symmetry lines, where the bands cross at points  $W_1$  and  $W_2$  in the Brillouin zone. Near the Weyl points, the bands are linear along the  $k_z$  directions, but parabolic touched in the  $k_x$  and  $k_y$  directions. (d) The Chern number in the  $k_x$ - $k_y$  plane as a function of  $k_z$ . (e) The surface states on the (010) surface. Two Fermi arcs link the projections of the two Weyl points on the surface Brillouin zone.

shown in Fig. 3(b). The details about the  $U_0$  circuit module are presented in Appendix B.

The structure of a unit circuit cell is illustrated in Figs. 3(a) and 3(b). Using these unit cells, a three-dimensional circuit network with translational symmetry can be connected according to the tight-binding Hamiltonian Eq. (4). The Kirchhoff's equations for the circuit network can be written as

$$(h_1(\mathbf{k}) \oplus H_{N=1}^{\text{circuit}}(\mathbf{k}))\tilde{\mathbf{v}} = \omega^{-2}(0 \oplus I_2)\tilde{\mathbf{v}} \quad (5)$$

in the pseudospin space, where  $\oplus$  stands for direct sum of the constant representation space and the pseudospin space of the  $C_3$  symmetry group,  $\tilde{\mathbf{v}} = (\tilde{v}_1, \tilde{v}_2, \tilde{v}_3)^T$  are the node voltages in the basis of the eigenfunctions of the  $C_3$  symmetry group.  $H_{N=1}^{\text{circuit}}(\mathbf{k}) = \sum_{i=0}^3 d_i(\mathbf{k})\sigma_i$  is the Hamiltonian in the pseudospin space, where  $d_0(\mathbf{k}) = \frac{22}{3}LC_a$ ,  $d_1(\mathbf{k}) - id_2(\mathbf{k}) = -\frac{LC_a}{3}(\cos k_x - i\sqrt{3}\cos k_y)$  and  $d_3(\mathbf{k}) = -\frac{2\sqrt{3}}{3}L(C_a(\sin k_x + \sin k_y + \sin k_z) + \frac{1}{2R_m\omega})$ .  $R_m$ ,  $C_a$ , and  $L$  are parameters of the

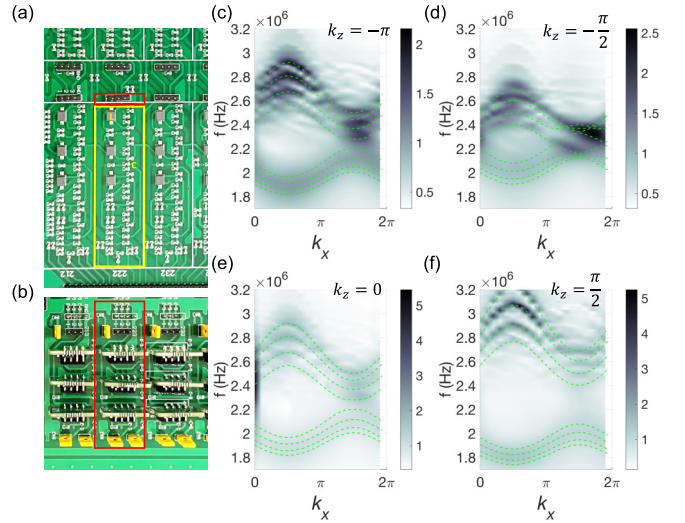


FIG. 6. The printed circuit board and experimentally observed edge states for the  $N = 2$  Weyl circuit. (a) Unit cell of the printed circuit board fabricated according to Figs. 5(a) and 5(b). The yellow box indicates the connection modules and the inductors. The red box indicates the interface for the  $U_0$  module. (b) The printed circuit board of the  $U_0$  module. (c)–(f) The experimentally measured band structure for  $k_z = -\pi, -\pi/2, 0$  and  $\pi/2$ . The black color represents the experimental data. The green curve is the computed band structure of a slab with four cells in the  $y$  direction. The  $k = -\pi$  and  $k = 0$  planes are close to the Weyl points, where exists small gap in the band structure. For the  $k = -\pi/2$  subsystem, two edge states cross the gap. The exciting signal source is connected to the cell at  $y = 4$ . Therefore, only the edge states localized at this boundary can be detected, while the edge states at the  $y = 1$  boundary cannot be detected. For  $k_z = \pi/2$ , there are no edge states in the gap.

components. More details about the circuit are presented in Appendix B.

We focus on  $H_{N=1}^{\text{circuit}}(\mathbf{k})$  in Eq. (5), where the term containing  $R_m$  originates from the  $U_0$  module. If this module is not included, the circuit consists of only two types of devices, capacitors, and inductors, and the effective Hamiltonian is given as  $H_0(\mathbf{k}) = H_{N=1}^{\text{circuit}}(\mathbf{k}) - H_{U_0}$ , where  $H_{U_0} = -\frac{\sqrt{3}L}{3R_m\omega}\sigma_3$ . The effective Hamiltonian  $H_0(\mathbf{k})$  is time-reversal invariant, i.e.,  $TH_0(\mathbf{k})T^{-1} = H_0(-\mathbf{k})$ , where  $T = \sigma_1K$  and  $K$  is complex conjugation operator. The  $U_0$  module contains resistors and active devices; the operational amplifiers break the time-reversal symmetry, i.e.,  $TH_{U_0}T^{-1} \neq H_{U_0}$ . As a result, the whole circuit network breaks the time-reversal symmetry, ensuring a single pair of Weyl points in the band structure. In Fig. 3(c), we show the calculated frequency dispersion of  $H_{N=1}^{\text{circuit}}(\mathbf{k})$ . One can see that the bands cross at Weyl points  $W_1$  and  $W_2$  and have a linear dispersion in directions  $k_x$ ,  $k_y$ , and  $k_z$  near the crossing points. The term  $h_1(\mathbf{k})$  in Eq. (5) is not our concern. By selecting the appropriate parameters, it is possible to move the eigenfrequencies of  $h_1(\mathbf{k})$  away from the eigenfrequencies of  $H_{N=1}^{\text{circuit}}(\mathbf{k})$ . The topological charge of the Weyl point can be revealed by the topological number  $C(k_z)$ , which is the Chern number in the  $k_x$ - $k_y$  space, with  $k_z$  as the parameter. The calculated Chern number  $C(k_z)$  is shown in Fig. 3(d), where it increases by one at point  $W_1$  and

decreases by one at point  $W_2$ . Thus, the topological charge of the Weyl point  $W_{1,2}$  equals  $\pm 1$ . In three-dimensional Weyl materials, when the Weyl points are projected onto the material's surface, it can be observed that Fermi arcs connect the Weyl points with opposite chirality. The number of Fermi arcs is determined by the topological charge of the projected Weyl points. This bulk-surface correspondence property is frequently used to identify the topological nature of Weyl materials in experiments. The surface states in the (010) direction calculated from the model Hamiltonian Eq. (5) are shown in Fig. 3(e). The two Weyl points are linked with a Fermi arc, which is consistent with the topological charge of the Weyl points.

In our design, the Weyl points are not protected by symmetry. Hence their positions are not at the high-symmetry points but the general points in the Brillouin zone. Therefore, a very dense  $k$  point, i.e., a large real space network, is required to observe the Weyl points in the experiment. The Chern number  $C(k_z)$  changes at the Weyl point, and the value of its change is just the topological charge of the Weyl point. This property makes it possible to confirm the existence of the Weyl point and its topological charge by measuring  $C(k_z)$ . Experimentally, we can measure the number of edge states of the two-dimensional subsystem parameterized by  $k_z$  in the three-dimensional system to obtain the Chern number  $C(k_z)$  with a relatively small circuit network. Based on this idea, we fabricate the printed circuit board (PCB) containing  $20 \times 4 \times 4$  unit cells with periodic boundary conditions in the  $x$  and  $z$  directions and open boundary conditions in the  $y$  direction. The structure of a unit circuit cell is shown in Figs. 4(a) and 4(b). By performing the AC sweep analysis, we obtain the band structure of the circuit network as shown in Figs. 4(c)–4(f). The band structure has a clear gap for  $k_z = \pi/2$ , and there are no edge states. The experimental results are consistent with the model calculation results as  $C(k_z) = 0$  and the surface states in this area do not have a Fermi arc. For  $k_z = -\pi/2$ , there is an edge state crossing through the bandgap, which is consistent with the Chern number  $C(k_z) = 1$  calculated from model Hamiltonian Eq. (5). Therefore, a Weyl point exists in the area between  $k_z = -\pi/2$  and  $k_z = \pi/2$ , which has a topological charge equal to one. Increasing the number of circuit cells enables a more accurate measurement of the location of the Weyl point in the three-dimensional Brillouin zone. More details about the experiment are presented in Appendix E.

#### IV. THE WEYL CIRCUIT WITH TOPOLOGICAL CHARGE EQUAL TO $\pm 2$

We now provide the design scheme for the ideal unconventional Weyl state with topological charge  $N = 2$ . In this case, the Hamiltonian Eq. (1) can be explored with a square lattice described by a tight-binding Hamiltonian

$$H_{N=2} = \sum_{i,j} \sum_{k=0}^7 (c_{i+\delta_k,j}^\dagger \hat{U}_k c_{i,j} + \text{H.c.}), \quad (6)$$

where  $i$  and  $j$  indicate the lattice sites,  $\delta_k$  are hopping vectors,  $\hat{U}_k$  are spin-orbit coupling operators, and their expressions are given in Table I. As in the  $N = 1$  case, these operators can be obtained by using the basic connection modules given in

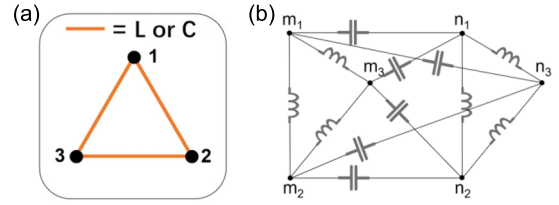


FIG. 7. Construct pseudospin space and matrix-form hopping in the circuit. (a) Three components (capacitors or inductors) with the same parameters are connected head to tail to form a triangle. The nodes are labeled 1–3. (b) Two triangle cells,  $m$  and  $n$ , are connected by module  $m_{-ox}$ .

Figs. 2(b)–2(d). The  $\hat{U}_0$  term characterizes the coupling within the unit cell that can be realized by using the inverting operational amplifier as shown in Fig. 5(b). The structure of a unit circuit cell for the Weyl circuit is shown in Figs. 5(a) and 5(b). Using these unit cells, a three-dimensional circuit network with translational symmetry can be connected according to the tight-binding Hamiltonian Eq. (6). The Kirchhoff's equations for the circuit network are given as

$$(h_1(\mathbf{k}) \oplus H_{N=2}^{\text{circuit}}(\mathbf{k})) \tilde{\mathbf{v}} = \omega^{-2} (0 \oplus I_2) \tilde{\mathbf{v}}, \quad (7)$$

in the pseudospin space, where  $H_{N=2}^{\text{circuit}}(\mathbf{k}) = \sum_{i=0}^3 d_i(\mathbf{k}) \sigma_i$  is the Hamiltonian in the pseudospin space, where  $d_0(\mathbf{k}) = \frac{28}{3} C_a$ ,  $d_1(\mathbf{k}) - id_2(\mathbf{k}) = -\frac{LC_a}{3} (\cos k_x - i\sqrt{3} \cos k_y)^2$ ,  $d_3(\mathbf{k}) = -\frac{2\sqrt{3}L}{3} (C_a (\sin k_x + \sin k_y + \sin k_z) + \frac{1}{2R_m\omega})$ .  $R_m$ ,  $C_a$ , and  $L$  are parameters of the components. In Fig. 5(c), we show the calculated band structure of  $H_{N=2}^{\text{circuit}}(\mathbf{k})$ . The two bands cross at points  $W_1$  and  $W_2$  and have a linear dispersion to  $k_z$ , but parabolic touched in the  $k_x$  and  $k_y$  directions. The Chern number  $C(k_z)$  as a function of  $k_z$  is shown in Fig. 5(d). It increases by two at point  $W_1$  and decreases by two at point  $W_2$ . Thus, the topological charge is equal to  $\pm 2$  at the Weyl points  $W_{1,2}$ . The surface states on the (010) direction calculated from model Hamiltonian Eq. (7) are shown in Fig. 5(e), where two Fermi arcs connect the projections of the two Weyl points. More details about the circuit are presented in Appendix C.

To verify the above theoretical results, we fabricate PCB containing  $20 \times 4 \times 4$  unit cells with periodic boundary conditions in the  $x$  and  $z$  directions and open boundary conditions in the  $y$  direction. The structure of the unit circuit cell is shown in Figs. 6(a) and 6(b). By performing AC sweep analysis, we obtain the band structure of the circuit network as shown in Figs. 6(c)–6(f). The band structure shows a clear gap for  $k_z = \pi/2$ , and there are no edge states, which is consistent with

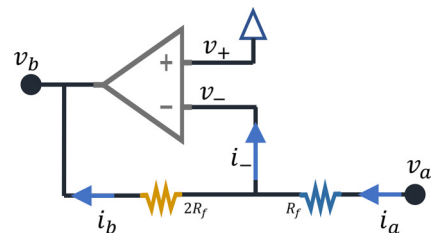


FIG. 8. Schematic of the operational inverting amplifier.

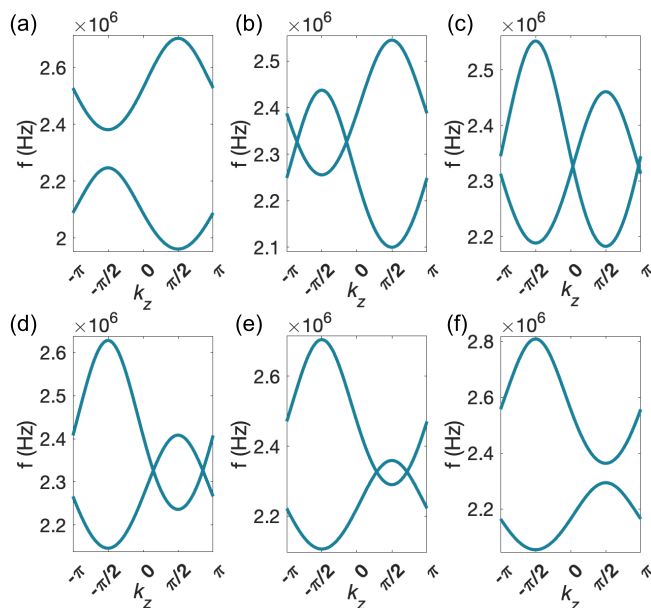


FIG. 9. The band structure as a function of  $R_m$  for Weyl circuit with  $N = 1$ . The  $k$ -point path passes through the point  $(k_x, k_y) = (-\pi/2, -\pi/2)$  and along the  $k_z$  direction. (a) for  $R_m = 50 \Omega$ , (b) for  $R_m = 70 \Omega$ , (c) for  $R_m = 90 \Omega$ , (d) for  $R_m = 110 \Omega$ , (d) for  $R_m = 140 \Omega$ , and (f) for  $R_m = 220 \Omega$ . The parameter of capacitance is  $C_a = 0.2$  nF and the parameter of inductance is  $L = 2.7 \mu\text{H}$ .

the model calculation results as  $C(k_z) = 0$  and the surface states in this area do not have a Fermi arc. For  $k_z = -\pi/2$ , two edge states are crossing through the band gap, which is consistent with the Chern number  $C(k_z) = 2$  calculated from model Hamiltonian Eq. (7). Therefore, a Weyl point with a topological charge equal to two exists in the area between  $k_z = -\pi/2$  and  $k_z = \pi/2$ .

For topological charge  $N$  equal to three or higher values, the design scheme is similar to the cases of  $N$  equal to 1 and 2, except that longer and more hopping terms are required, which increases the complexity of the circuit structures. As indicated in Eq. (1), the increase of connection complexity is only on the  $x$ - $y$  plane. The connections in the  $z$  direction are the same for any  $N$ . In Appendix D, we give details of the Weyl circuit for  $N = 3, 4$ , and 5.

## V. CONCLUSION

This paper provides a model Hamiltonian with long-range three-dimensional spin-orbit coupling instead of symmetry to design the ideal conventional and unconventional Weyl states. We verify our theory in circuit networks, where two types of circuit modules are designed. The first one is the connection modules that enable the implementation of long-range spin-orbit coupling. The second one is the on-site module that breaks the time-reversal symmetry. We can use these modules to realize Weyl states with a topological charge equal to an arbitrary integer. Our design scheme is highly generalizable. It can be used to construct topological Chern insulating states with an arbitrary Chern number in two-dimensional systems and be extended to arbitrary spatial dimensions to implement states of matter that are difficult to access in solids.

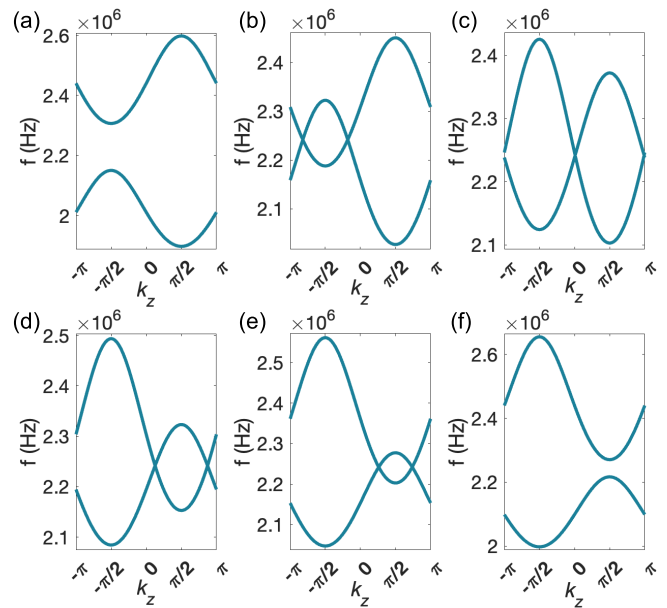


FIG. 10. Band structure as a function of  $R_m$  for Weyl circuit with  $N = 2$ . The  $k$ -point path passes through the point  $(k_x, k_y) = (-\pi/2, -\pi/2)$  and along the  $k_z$  direction. (a) For  $R_m = 50 \Omega$ , (b) for  $R_m = 70 \Omega$ , (c) for  $R_m = 90 \Omega$ , (d) for  $R_m = 110 \Omega$ , (e) for  $R_m = 140 \Omega$ , and (f) for  $R_m = 220 \Omega$ . The parameter of capacitance is  $C_a = 0.2$  nF and the parameter of inductance is  $L = 2.7 \mu\text{H}$ .

## ACKNOWLEDGMENTS

This work was supported by the National Natural Science Foundation of China (No. 12274328) and the Beijing National Laboratory for Condensed Matter Physics.

## APPENDIX A: PSEUDOSPIN SPACE AND SPIN-ORBIT COUPLING IN CIRCUIT

For the circuit illustrated in Fig. 7(a), three identical components (capacitors or inductors) are connected head to tail to form a triangle with  $C_3$  rotational symmetry. As shown in Table II, the  $C_3$  symmetry has an irreducible two-dimensional representation with basis functions that are complex conjugates of each other. Therefore, we can choose these twofold degenerate eigenstates as the basis functions for the pseudospin space. We use the inductor circuit as an example to present the derived details. The Kirchhoff's current equations

TABLE II. Character table for  $C_3$  point group, where  $\epsilon = e^{i2\pi/3}$ . The two sets of characters in representation  $E$  are complex conjugates of each other. For systems with time-reversal symmetry, representation  $E$  is twofold degeneracy.

$C_3$	$E$	$C_3$	$C_3^2$
$A$	1	1	1
$E$	1	$\epsilon$	$\epsilon^*$
	1	$\epsilon^*$	$\epsilon$

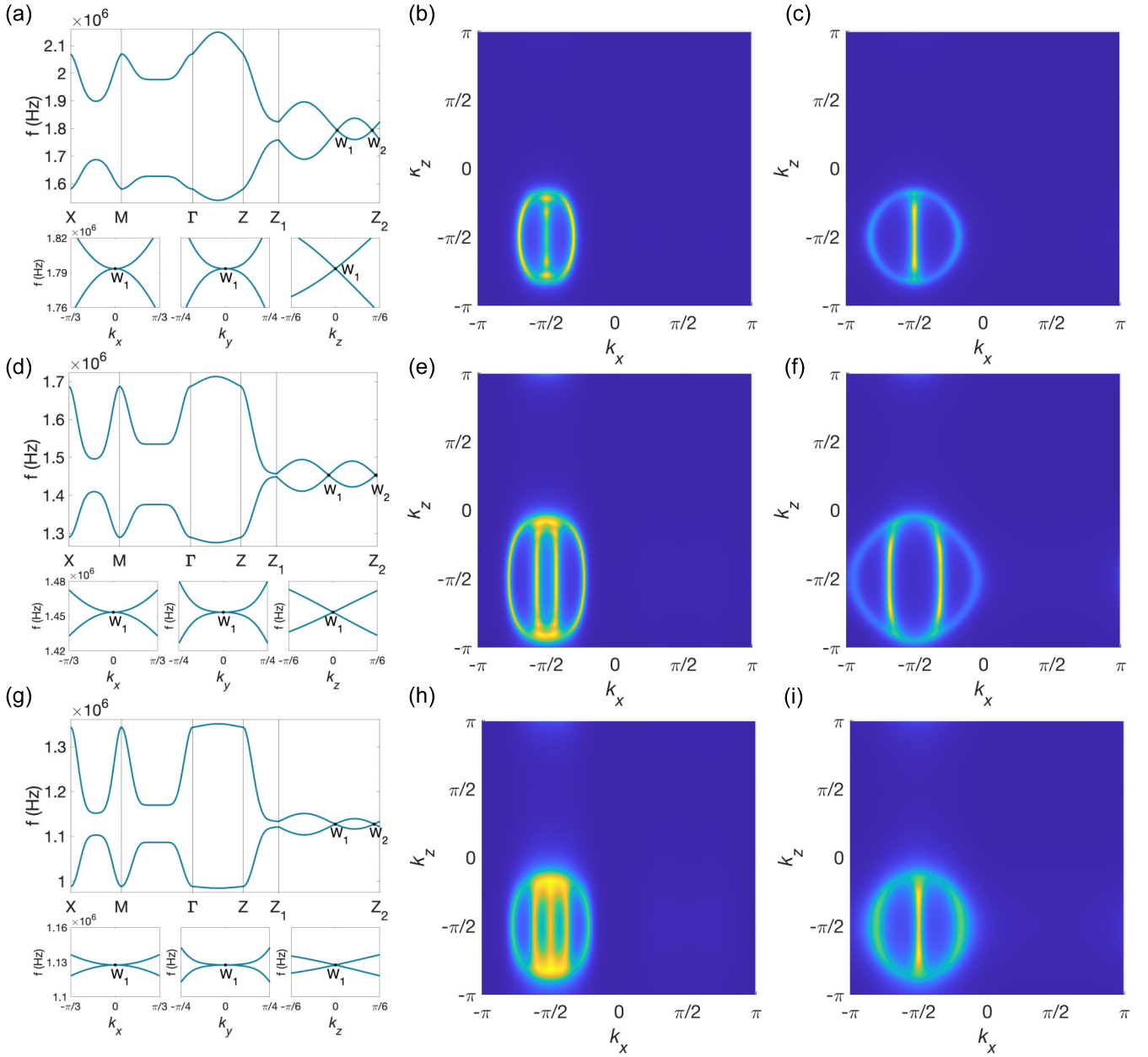


FIG. 11. (a) Eigenfrequency dispersion of the  $N = 3$  Weyl circuit along high-symmetry lines. (b) The (100) surface states of the Weyl state with topological charge equal to three. There are three Fermi arcs connecting the projection of the Weyl points. (c) The (010) surface states for  $N = 3$  Weyl circuit. (d) Eigenfrequency dispersion of the  $N = 4$  Weyl circuit. (e)–(f) The (100) and (010) surface states of the  $N = 4$  Weyl state. (g)–(i) Band structure and the (100) and (010) surface states of the  $n = 5$  Weyl state. the Fermi arcs on the (010) surface are overlapping and only three are visible. In the above three Weyl circuits, the parameter of the inductor in the pseudospin modules is  $L = 2.7 \mu\text{H}$ , and the parameter of the capacitor is  $C_a = 0.2 \text{ nF}$ . The resistor in the  $U_0$  module is  $R_f = 90 \Omega$  for  $N = 3$  and  $R_f = 130 \Omega$  for  $N = 4$  and 5.

for the circuit in Fig. 7(a) can be written as

$$\begin{bmatrix} i_1 \\ i_2 \\ i_3 \end{bmatrix} = \frac{1}{i\omega L} \begin{bmatrix} -2 & 1 & 1 \\ 1 & -2 & 1 \\ 1 & 1 & -2 \end{bmatrix} \begin{bmatrix} v_1 \\ v_2 \\ v_3 \end{bmatrix}, \quad (\text{A1})$$

where  $v_{1,2,3}$  are the voltages on the nodes, and  $i_{1,2,3}$  are the currents flowing into each node.  $L$  is the inductance of the inductors.  $\omega$  is the frequency of the AC signal. We abbreviate the  $3 \times 3$  admittance matrix on the right-hand side of Eq. (A1)

as  $M_L$ . Diagonalizing  $M_L$ , we obtain

$$U^\dagger M_L U = \Lambda, \quad (\text{A2})$$

where the eigenfunctions  $U$  and eigenfrequencies  $\Lambda$  are given as

$$U = \frac{1}{\sqrt{3}} \begin{bmatrix} 1 & \epsilon & \epsilon^* \\ 1 & \epsilon^* & \epsilon \\ 1 & 1 & 1 \end{bmatrix}, \quad \Lambda = - \begin{bmatrix} 0 & & \\ & 3 & \\ & & 3 \end{bmatrix}, \quad (\text{A3})$$

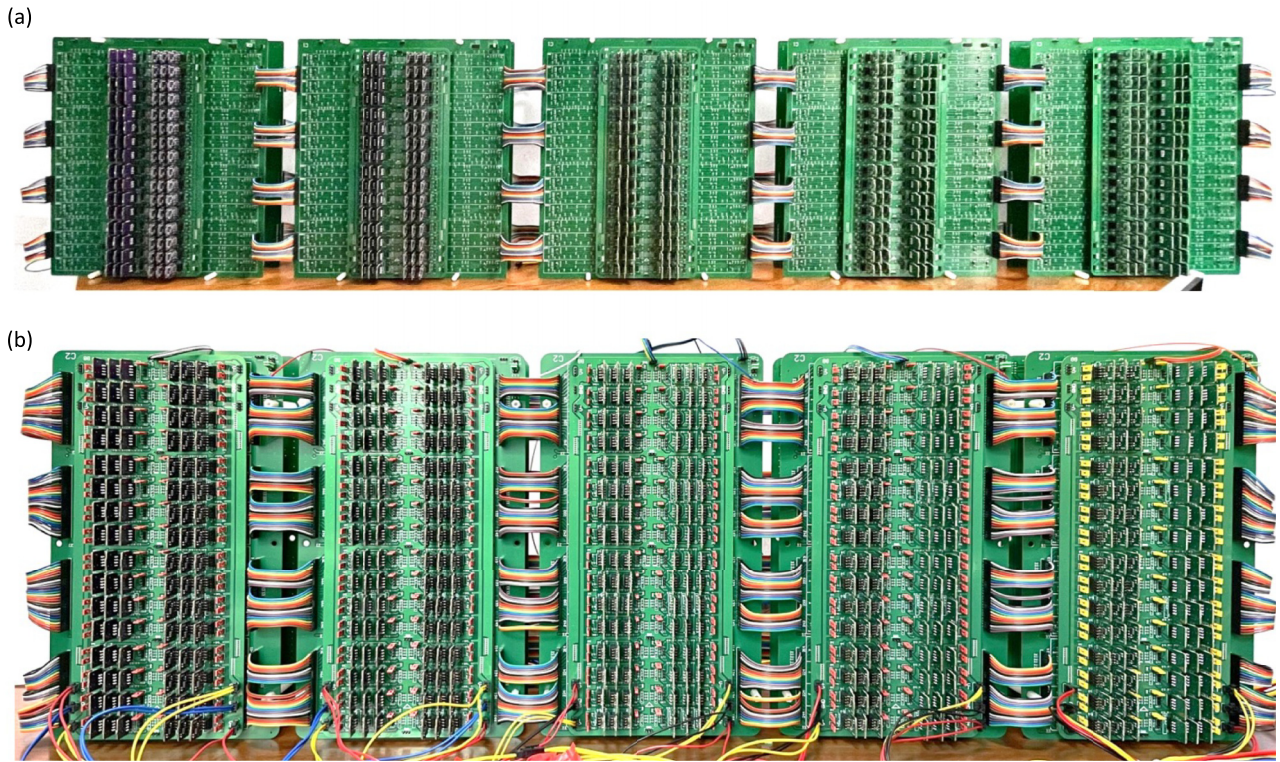


FIG. 12. (a), (b) The printed circuit boards designed according to the model Hamiltonian Eqs. (4) and (6), which are assembled together to form the  $20 \times 4 \times 4$  Weyl circuit systems.

and  $\epsilon = e^{i2\pi/3}$ . The twofold degenerate states in Eq. (A3), i.e.,  $\phi_{s_1} = \frac{1}{\sqrt{3}}(\epsilon, \epsilon^*, 1)^T$  and  $\phi_{s_2} = \frac{1}{\sqrt{3}}(\epsilon^*, \epsilon, 1)^T$ , can be chosen as the basis functions of the pseudospin space.  $\phi_0 = \frac{1}{\sqrt{3}}(1, 1, 1)^T$  is the basis function for the constant representation space.

Now, we provide connection modules that generate Pauli matrix-type couplings. We take module  $m_{-\sigma_1}$ , which generates a  $-\sigma_1$  type coupling, as an example to show the derivation details. Ohm's law indicates the sum of the currents entering each node in Fig. 7(b) are given as

$$i_{m_1} = y_L(v_{m_3} + v_{m_2} - 2v_{m_1}) + y_{C_a}(v_{n_3} - v_{m_1}) + y_{C_a}(v_{n_1} - v_{m_1}), \quad (\text{A4})$$

$$i_{m_2} = y_L(v_{m_1} + v_{m_3} - 2v_{m_2}) + y_{C_a}(v_{n_3} - v_{m_2}) + y_{C_a}(v_{n_2} - v_{m_2}), \quad (\text{A5})$$

$$i_{m_3} = y_L(v_{m_1} + v_{m_2} - 2v_{m_3}) + y_{C_a}(v_{n_1} - v_{m_3}) + y_{C_a}(v_{n_2} - v_{m_3}), \quad (\text{A6})$$

$$i_{n_1} = y_L(v_{n_3} + v_{n_2} - 2v_{n_1}) + y_{C_a}(v_{m_3} - v_{n_1}) + y_{C_a}(v_{m_1} - v_{n_1}), \quad (\text{A7})$$

$$i_{n_2} = y_L(v_{n_1} + v_{n_3} - 2v_{n_2}) + y_{C_a}(v_{m_3} - v_{n_2}) + y_{C_a}(v_{m_2} - v_{n_2}), \quad (\text{A8})$$

$$i_{n_3} = y_L(v_{n_1} + v_{n_2} - 2v_{n_3}) + y_{C_a}(v_{m_1} - v_{n_3}) + y_{C_a}(v_{m_2} - v_{n_3}), \quad (\text{A9})$$

where  $i_{m,n}$ ,  $v_{m,n}$ , and  $y_{L,C_a}$  are the currents, voltages, and admittance of the devices, respectively. In the stationary AC signal analysis,  $y_{C_a} = i\omega C_a$  for capacitors and  $y_L = 1/i\omega L$  for inductors. Writing the above equations into matrix form, we get

$$\begin{bmatrix} \mathbf{i}_m \\ \mathbf{i}_n \end{bmatrix} = \begin{bmatrix} \frac{1}{i\omega L} M_L - i\omega 2C_a I_3 & i\omega C_a M_{-\sigma_1} \\ i\omega C_a M_{-\sigma_1}^T & \frac{1}{i\omega L} M_L - i\omega 2C_a I_3 \end{bmatrix} \begin{bmatrix} \mathbf{v}_m \\ \mathbf{v}_n \end{bmatrix}, \quad (\text{A10})$$

where  $\mathbf{i}_{m(n)} = (i_{m(n)_1}, i_{m(n)_2}, i_{m(n)_3})^T$ ,  $\mathbf{v}_{m(n)} = (v_{m(n)_1}, v_{m(n)_2}, v_{m(n)_3})^T$ ,  $M_L$  is defined in Eq. (A1), and  $I_3$  is the identity matrix. Matrix  $M_{-\sigma_1}$  corresponds to the connection module  $m_{-\sigma_1}$ , which is given as

$$M_{-\sigma_1} = \begin{pmatrix} 1 & 0 & 1 \\ 0 & 1 & 1 \\ 1 & 1 & 0 \end{pmatrix}. \quad (\text{A11})$$

The  $6 \times 6$  matrix on the right-hand side of Eq. (A10) is the admittance matrix. With no external current source, the sum of the currents entering each circuit node equals zero, therefore Eq. (A10) can be formulated as

$$\begin{bmatrix} -2I_3 & M_{-\sigma_1} \\ M_{-\sigma_1}^T & -2I_3 \end{bmatrix} \begin{bmatrix} \mathbf{v}_m \\ \mathbf{v}_n \end{bmatrix} = \frac{1}{\omega^2 LC_a} \begin{bmatrix} M_L & 0 \\ 0 & M_L \end{bmatrix} \begin{bmatrix} \mathbf{v}_m \\ \mathbf{v}_n \end{bmatrix}. \quad (\text{A12})$$

Using the transformation matrix  $U$  given in Eq. (A3), we obtain

$$\begin{bmatrix} -2I_3 & U^\dagger M_{-\sigma_1} U \\ U^\dagger M_{-\sigma_1}^T U & -2I_3 \end{bmatrix} \begin{bmatrix} \tilde{\mathbf{v}}_m \\ \tilde{\mathbf{v}}_n \end{bmatrix} = \frac{\Lambda}{\omega^2 LC_a} \begin{bmatrix} \tilde{\mathbf{v}}_m \\ \tilde{\mathbf{v}}_n \end{bmatrix}, \quad (\text{A13})$$

where  $\tilde{v}_{m(n)} = U^\dagger v_{m(n)}$ , and

$$U^\dagger M_{-\sigma_1} U = \begin{bmatrix} 2 & 0 & 0 \\ 0 & 0 & -1 \\ 0 & -1 & 0 \end{bmatrix} = 2 \oplus -\sigma_1. \quad (\text{A14})$$

In this paper, the currents and voltages with a tilde above take the eigenfunctions of the  $C_3$  symmetry group as basis functions, and those without a tilde refer to currents and voltages at the circuit nodes. For the twofold degenerate states in Eq. (A13), tunneling from cell  $n$  to cell  $m$  is characterized by a Pauli matrix  $-\sigma_1$ . Using the same method, we can design the connection modules that connect cells  $m$  and  $n$ , with coupling matrices in the form of  $\pm\sigma_{1,2}$  and  $\pm i\sigma_3$ . The results are listed below:

$$M_{+\sigma_1} = \begin{pmatrix} 0 & 1 & 0 \\ 1 & 0 & 0 \\ 0 & 0 & 1 \end{pmatrix}, \quad U^\dagger M_{+\sigma_1} U = 1 \oplus \sigma_1, \quad (\text{A15})$$

$$M_{-\sigma_1} = \begin{pmatrix} 1 & 0 & 1 \\ 0 & 1 & 1 \\ 1 & 1 & 0 \end{pmatrix}, \quad U^\dagger M_{-\sigma_1} U = 2 \oplus (-\sigma_1), \quad (\text{A16})$$

$$M_{+\sigma_2} = \begin{pmatrix} 0 & 1 & 2 \\ 1 & 2 & 0 \\ 2 & 0 & 1 \end{pmatrix}, \quad U^\dagger M_{+\sigma_2} U = 3 \oplus \sqrt{3}\sigma_2, \quad (\text{A17})$$

$$M_{-\sigma_2} = \begin{pmatrix} 2 & 1 & 0 \\ 1 & 0 & 2 \\ 0 & 2 & 1 \end{pmatrix}, \quad U^\dagger M_{-\sigma_2} U = 3 \oplus (-\sqrt{3}\sigma_2), \quad (\text{A18})$$

$$M_{+i\sigma_3} = \begin{pmatrix} 1 & 2 & 0 \\ 0 & 1 & 2 \\ 2 & 0 & 1 \end{pmatrix}, \quad U^\dagger M_{+i\sigma_3} U = 3 \oplus i\sqrt{3}\sigma_3, \quad (\text{A19})$$

$$M_{-i\sigma_3} = \begin{pmatrix} 1 & 0 & 2 \\ 2 & 1 & 0 \\ 0 & 2 & 1 \end{pmatrix}, \quad U^\dagger M_{-i\sigma_3} U = 3 \oplus (-i\sqrt{3}\sigma_3). \quad (\text{A20})$$

## APPENDIX B: WEYL CIRCUIT WITH TOPOLOGICAL CHARGE EQUAL TO $\pm 1$

This Appendix gives details of the Weyl circuit with topological charge equal to  $\pm 1$ . The admittance matrix of the Kirchhoff's equation for the three-dimensional circuit network constructed with the unit cell of Figs. 3(a) and 3(b) can be written as

$$\begin{aligned} Y = & y_L M_L + y_{C_a} e^{ik \cdot \delta_1} (M_{\sigma_x} + M_{-i\sigma_z}) + y_{C_a} e^{-ik \cdot \delta_1} (M_{\sigma_x} + M_{-i\sigma_z}) \\ & + y_{C_a} e^{ik \cdot \delta_2} (M_{\sigma_y} + M_{-i\sigma_z}) \\ & + y_{C_a} e^{-ik \cdot \delta_2} (M_{\sigma_y} + M_{-i\sigma_z}) + y_{C_a} e^{ik \cdot \delta_3} M_{-i\sigma_z} \\ & + y_{C_a} e^{-ik \cdot \delta_3} M_{-i\sigma_z} - 22y_{C_a} I_3 + y_0 M_0, \end{aligned} \quad (\text{B1})$$

where  $M_{\sigma_i}$  are the admittance matrices corresponding to the connection modules. The last term  $y_0 M_0$  is for the on-site module [the  $U_0$  module in Fig. 3(b)]. In the following, we present the schemes for the design of the on-site module.

We design the on-site module by using the operational inverting amplifiers. The inverting amplifier is shown in Fig. 8. For an ideal operational amplifier, we have  $v_+ = v_- = 0$  and  $i_- = 0$ . This results in  $v_a/R_f = -v_b/(2R_f)$ , i.e.,  $v_b = -2v_a$ .

Using the voltage-current relationship of the operational inverting amplifiers, the currents flowing into the three nodes in Fig. 3(b) can be calculated as

$$i_1 = (-2v_3 - v_1)/R_m, \quad (\text{B2})$$

$$i_2 = (-2v_1 - v_2)/R_m, \quad (\text{B3})$$

$$i_3 = (-2v_2 - v_3)/R_m. \quad (\text{B4})$$

In the above derivation, we choose  $R_f \gg R_m$ , so the current flowing through the  $R_f$  branch can be ignored. Taking the matrix form of the above three equations, the admittance matrix of the  $U_0$  module is given by

$$y_0 M_0 = -\frac{1}{R_m} \begin{bmatrix} 1 & 0 & 2 \\ 2 & 1 & 0 \\ 0 & 2 & 1 \end{bmatrix}. \quad (\text{B5})$$

The Kirchhoff's equation  $\mathbf{i} = Y \mathbf{v}$  can be reduced to

$$(h_1(\mathbf{k}) \oplus H_{N=1}^{\text{circuit}}(\mathbf{k})) \tilde{\mathbf{v}} = \omega^{-2} (0 \oplus I_2) \tilde{\mathbf{v}}, \quad (\text{B6})$$

with no external input currents, where  $\mathbf{v} = (v_1, v_2, v_3)$  are the voltage at the nodes in the unit cell,  $\tilde{\mathbf{v}} = U^\dagger \mathbf{v}$ , and  $U$  is defined in Eq. (A3).  $H_{N=1}^{\text{circuit}}(\mathbf{k}) = \sum_{i=0}^3 d_i(\mathbf{k}) \sigma_i$  is the Weyl Hamiltonian in the pseudospin space, where

$$d_0(\mathbf{k}) = \frac{22}{3} LC_a, \quad (\text{B7})$$

$$d_1(\mathbf{k}) - id_2(\mathbf{k}) = -\frac{LC_a}{3} (\cos k_x - i\sqrt{3} \cos k_y), \quad (\text{B8})$$

$$d_3(\mathbf{k}) = -\frac{2\sqrt{3}L}{3} \left( C_a (\sin k_x + \sin k_y + \sin k_z) + \frac{1}{2R_m \omega} \right). \quad (\text{B9})$$

The energy bands of  $H_{N=1}^{\text{circuit}}(\mathbf{k})$  are shown in Fig. 3(c). Here, we show that the appearance and disappearance of the Weyl point can be controlled by the parameter  $R_m$ . As shown in Fig. 9, with the increase of  $R_m$ , the frequency bands change from insulator to Weyl semimetal and then to the insulator. The parameter  $R_m$  guarantees the existence of two Weyl points in a wide range of values.

$h_1(\mathbf{k})$  is the Hamiltonian in the constant representation space of the  $C_3$  symmetry group, which is given as

$$h_1(\mathbf{k}) = \frac{3}{R_m} + i\omega C_a (22 - 7 \cos k_x - 9 \cos k_y - 6 \cos k_z). \quad (\text{B10})$$

It is easy to verify that the real part of the eigenfrequency of  $h_1$  is equal to 0, and the imaginary part is greater than 0, which means that the electrical signal decays with time and it is a stable solution of the system.

## APPENDIX C: WEYL CIRCUIT WITH TOPOLOGICAL CHARGE EQUAL TO $\pm 2$

In this Appendix, we give details of the Weyl circuit with topological charge equal to  $\pm 2$ . The admittance matrix of the Kirchhoff's equation for the three-dimensional circuit network built with the unit cell of Figs. 5(a) and 5(b) can be

TABLE III. The hopping vectors and the corresponding hopping matrices for the Weyl circuit with topological charges equal to  $\pm 3$ .  $\hat{x}$ ,  $\hat{y}$ , and  $\hat{z}$  denote the lattice vectors in the  $x$ ,  $y$ , and  $z$  directions, respectively.

	$k$	0	1	2	3
	$\delta_k$	0	$\hat{x}$	$\hat{y}$	$\hat{z}$
	$\hat{U}_k$	$m_0\sigma_3$	$(\frac{3}{8}\alpha^3 - \frac{3}{4}\alpha\beta^2)\sigma_1 - \frac{1}{2}\gamma_1\sigma_3$	$(\frac{3}{4}\alpha^2\beta - \frac{3}{8}\beta^3)\sigma_2 - \frac{1}{2}\gamma_2\sigma_3$	$-\frac{1}{2}\gamma_3\sigma_3$
$N = 3$	$k$	4	5	6	7
	$\delta_k$	$3\hat{x}$	$3\hat{y}$	$\hat{x} + 2\hat{y}$	$\hat{x} - 2\hat{y}$
	$\hat{U}_k$	$\frac{1}{8}\alpha^3\sigma_1$	$-\frac{1}{8}\beta^3\sigma_2$	$-\frac{3}{8}\alpha\beta^2\sigma_1$	$-\frac{3}{8}\alpha\beta^2\sigma_1$
	$k$	8	9		
	$\delta_k$	$2\hat{x} + \hat{y}$	$2\hat{x} - \hat{y}$		
	$\hat{U}_k$	$\frac{3}{8}\alpha^2\beta\sigma_2$	$\frac{3}{8}\alpha^2\beta\sigma_2$		

TABLE IV. The hopping vectors and the corresponding hopping matrices for the Weyl circuit with topological charges equal to  $\pm 4$ .

	$k$	0	1	2	3
	$\delta_k$	0	$\hat{x}$	$\hat{y}$	$\hat{z}$
	$\hat{U}_k$	$(\frac{3}{8}\alpha^4 - \frac{3}{2}\alpha^2\beta^2 + \frac{3}{8}\beta^4)\sigma_1 + m_0\sigma_3$	$-\frac{1}{2}\gamma_1\sigma_3$	$-\frac{1}{2}\gamma_2\sigma_3$	$-\frac{1}{2}\gamma_3\sigma_3$
$N = 4$	$k$	4	5	6	7
	$\delta_k$	$2\hat{x}$	$2\hat{y}$	$4\hat{x}$	$4\hat{y}$
	$\hat{U}_k$	$(\frac{1}{4}\alpha^4 - \frac{3}{4}\alpha^2\beta^2)\sigma_1$	$(-\frac{3}{4}\alpha^2\beta^2 + \frac{1}{4}\beta^4)\sigma_1$	$\frac{1}{16}\alpha^4\sigma_1$	$\frac{1}{16}\beta^4\sigma_1$
	$k$	8	9	10	11
	$\delta_k$	$\hat{x} + \hat{y}$	$\hat{x} - \hat{y}$	$\hat{x} + 3\hat{y}$	$\hat{x} - 3\hat{y}$
	$\hat{U}_k$	$\frac{3}{4}(\alpha^3\beta - \alpha\beta^3)\sigma_2$	$\frac{3}{4}(\alpha^3\beta - \alpha\beta^3)\sigma_2$	$-\frac{1}{4}\alpha\beta^3\sigma_2$	$-\frac{1}{4}\alpha\beta^3\sigma_2$
	$k$	11	12	13	14
	$\delta_k$	$3\hat{x} - \hat{y}$	$3\hat{x} + \hat{y}$	$2\hat{x} - 2\hat{y}$	$2\hat{x} + 2\hat{y}$
	$\hat{U}_k$	$\frac{1}{4}\alpha^3\beta\sigma_2$	$\frac{1}{4}\alpha^3\beta\sigma_2$	$-\frac{3}{8}\alpha^2\beta^2\sigma_1$	$-\frac{3}{8}\alpha^2\beta^2\sigma_1$

TABLE V. The hopping vectors and the corresponding hopping matrices for the Weyl circuit with topological charges equal to  $\pm 5$ .  $p_1 = \frac{5}{16}\alpha^5 - \frac{15}{8}\alpha^3\beta^2 + \frac{15}{16}\alpha\beta^4$ , and  $p_2 = \frac{15}{16}\alpha^4\beta - \frac{15}{8}\alpha^2\beta^3 + \frac{5}{16}\beta^5$ .

	$k$	0	1	2
	$\delta_k$	0	$\hat{x}$	$\hat{y}$
	$\hat{U}_k$	$m_0\sigma_3$	$p_1\sigma_1 - \frac{1}{2}\gamma_1\sigma_3$	$p_2\sigma_2 - \frac{1}{2}\gamma_2\sigma_3$
$N = 5$	$k$	3	4	5
	$\delta_k$	$\hat{z}$	$3\hat{x}$	$3\hat{y}$
	$\hat{U}_k$	$-\frac{1}{2}\gamma_3\sigma_3$	$(\frac{5}{32}\alpha^5 - \frac{5}{8}\alpha^3\beta^2)\sigma_1$	$(-\frac{5}{8}\alpha^2\beta^3 + \frac{5}{32}\beta^5)\sigma_2$
	$k$	6	7	8
	$\delta_k$	$5\hat{x}$	$5\hat{y}$	$\hat{x} + 2\hat{y}$
	$\hat{U}_k$	$\frac{1}{32}\alpha^5\sigma_1$	$\frac{1}{32}\beta^5\sigma_2$	$(-\frac{15}{16}\alpha^3\beta^2 + \frac{5}{8}\alpha\beta^4)\sigma_1$
	$k$	9	10	11
	$\delta_k$	$\hat{x} - 2\hat{y}$	$\hat{x} + 4\hat{y}$	$\hat{x} - 4\hat{y}$
	$\hat{U}_k$	$(-\frac{15}{16}\alpha^3\beta^2 + \frac{5}{8}\alpha\beta^4)\sigma_1$	$\frac{5}{32}\alpha\beta^4\sigma_1$	$\frac{5}{32}\alpha\beta^4\sigma_1$
	$k$	12	13	14
	$\delta_k$	$2\hat{x} + \hat{y}$	$2\hat{x} - \hat{y}$	$2\hat{x} + 3\hat{y}$
	$\hat{U}_k$	$(\frac{5}{8}\alpha^4\beta - \frac{15}{16}\alpha^2\beta^3)\sigma_2$	$(\frac{5}{8}\alpha^4\beta - \frac{15}{16}\alpha^2\beta^3)\sigma_2$	$-\frac{5}{16}\alpha^2\beta^3\sigma_2$
	$k$	15	16	17
	$\delta_k$	$2\hat{x} - 3\hat{y}$	$3\hat{x} + 2\hat{y}$	$3\hat{x} - 2\hat{y}$
	$\hat{U}_k$	$-\frac{5}{16}\alpha^2\beta^3\sigma_2$	$-\frac{5}{16}\alpha^3\beta^2\sigma_1$	$-\frac{5}{16}\alpha^3\beta^2\sigma_1$
$k$	18	19		
$\delta_k$	$4\hat{x} + \hat{y}$	$4\hat{x} - \hat{y}$		
	$\hat{U}_k$	$\frac{5}{32}\alpha^4\beta\sigma_2$	$\frac{5}{32}\alpha^4\beta\sigma_2$	

written as

$$\begin{aligned}
 Y = & y_L M_L + y_{C_a} (e^{ik \cdot \delta_1} M_{-i\sigma_z} + e^{-ik \cdot \delta_1} M_{i\sigma_z}) \\
 & + y_{C_a} (e^{ik \cdot \delta_2} M_{-i\sigma_z} + e^{-ik \cdot \delta_2} M_{i\sigma_z}) \\
 & + y_{C_a} (e^{ik \cdot \delta_3} M_{-i\sigma_z} + e^{-ik \cdot \delta_3} M_{i\sigma_z}) \\
 & + \frac{1}{4} y_{C_a} (e^{ik \cdot \delta_4} M_{\sigma_x} + e^{-ik \cdot \delta_4} M_{\sigma_x}) \\
 & + \frac{3}{4} y_{C_a} (e^{ik \cdot \delta_5} M_{-\sigma_x} + e^{-ik \cdot \delta_5} M_{-\sigma_x}) \\
 & + \frac{1}{2} y_{C_a} (e^{ik \cdot \delta_6} M_{\sigma_y} + e^{-ik \cdot \delta_6} M_{\sigma_y}) \\
 & + \frac{1}{2} y_{C_a} (e^{ik \cdot \delta_7} M_{\sigma_y} + e^{-ik \cdot \delta_7} M_{\sigma_y}) - \frac{55}{2} y_{C_a} I_3 + y_0 M_0,
 \end{aligned} \tag{C1}$$

where  $M_{\sigma_i}$  are the admittance matrices corresponding to the connection modules, which are listed in the Eqs. (A15)–(A20). The last term  $y_0 M_0$  is for the on-site module (the  $U_0$ -module in Fig. 5(b)). In the following, we give the schemes for designing the on-site module.

Using the voltage-current relationship of the inverting amplifier as shown in Fig. 8, the currents flowing into the three nodes in Fig. 5(b) can be calculated as

$$i_1 = (-2v_3 - v_1)/R_m + i\omega C_a(-2v_2 - v_1)/2, \tag{C2}$$

$$i_2 = (-2v_1 - v_2)/R_m + i\omega C_a(-2v_1 - v_2)/2, \tag{C3}$$

$$i_3 = (-2v_2 - v_3)/R_m + i\omega 3C_a(0 - v_3)/2. \tag{C4}$$

Taking the matrix form of the above three equations, the admittance matrix of the circuit is obtained as

$$y_0 M_0 = -\frac{1}{R_m} \begin{bmatrix} 1 & 0 & 2 \\ 2 & 1 & 0 \\ 0 & 2 & 1 \end{bmatrix} + \frac{i\omega C_a}{2} \begin{bmatrix} -1 & -2 & 0 \\ -2 & -1 & 0 \\ 0 & 0 & -3 \end{bmatrix}. \tag{C5}$$

The Kirchhoff's equation  $\mathbf{i} = Y \mathbf{v}$  can be reduced to

$$(h_1(\mathbf{k}) \oplus H_{N=2}^{\text{circuit}}(\mathbf{k})) \tilde{\mathbf{v}} = \omega^{-2} (0 \oplus I_2) \tilde{\mathbf{v}}, \tag{C6}$$

with no external input currents, where  $H_{N=2}^{\text{circuit}}(\mathbf{k}) = \sum_{i=0}^3 d_i(\mathbf{k}) \sigma_i$  is the Chern insulator Hamiltonian in the pseudospin space with

$$d_0(\mathbf{k}) = \frac{28}{3} LC_a, \tag{C7}$$

$$d_1(\mathbf{k}) - id_2(\mathbf{k}) = -\frac{LC_a}{3} (\cos k_x - i\sqrt{3} \cos k_y)^2, \tag{C8}$$

$$d_3(\mathbf{k}) = -\frac{2\sqrt{3}L}{3} \left( C_a (\sin k_x + \sin k_y + \sin k_z) + \frac{1}{2R_m \omega} \right). \tag{C9}$$

The energy bands of  $H_{N=2}^{\text{circuit}}(\mathbf{k})$  are shown in Fig. 5(c). Here, we show that the appearance and disappearance of the Weyl points can be controlled by the parameter  $R_m$ . As shown in Fig. 10, with the increase of  $R_m$ , the frequency bands change from insulator to Weyl semimetal and then to the insulator. From the above discussion, it is clear that the Weyl points are not due to symmetry but to the band-inversion mechanism. The topological charge of the Weyl point is determined by the specific form of the long-range spin-orbit coupling.

$h_1(\mathbf{k})$  is the Hamiltonian in the constant representation space of the  $C_3$  symmetry group, which is calculated as

$$\begin{aligned}
 h_1(\mathbf{k}) = & \frac{3}{R_m} + \frac{1}{2} i\omega C_a (58 - \cos 2k_x \\
 & - 12 \cos k_y - 12 \cos k_x (1 + \cos k_y) \\
 & - 6 \cos 2k_y - 12 \cos k_z).
 \end{aligned} \tag{C10}$$

It is easy to verify that the real part of the eigenfrequency of  $h_1$  is equal to 0, and the imaginary part is greater than 0. It indicates that the electrical signal corresponding to the eigenfrequency decays with time and is a stable solution for the system.

#### APPENDIX D: WEYL CIRCUIT WITH TOPOLOGICAL CHARGE EQUAL TO $\pm 3$ , $\pm 4$ , and $\pm 5$

This Appendix presents the design of the Weyl circuit with a topological charge  $N$  equal to 3, 4, and 5. By the Fourier transformation, the hopping vectors and hopping matrices in real space for the Hamiltonian Eq. (1) are summarized in Tables III–V. Similar to the cases for  $N$  equaling 1 and 2, the hopping matrices in Tables III–V can be implemented with the connection modules in Figs. 2(b)–2(d) and the on-site modules in Fig. 3(b) or Fig. 5(b). The design scheme of the Weyl circuit for  $N$  equals 3, 4, 5, or higher is similar to  $N$  equals 1 and 2, except that the hopping distance and the number of hopping terms increase as  $N$  increases. Here we do not sketch the specific circuits but give the calculation results directly.

The effective Hamiltonian of the Weyl circuit is  $H_N^{\text{circuit}}(\mathbf{k}) = \sum_{i=0}^3 d_i(\mathbf{k}) \sigma_i$ , where

$$d_1(\mathbf{k}) - id_2(\mathbf{k}) = -\frac{LC_a}{3} (\cos k_x - i\sqrt{3} \cos k_y)^N, \tag{D1}$$

$$d_3(\mathbf{k}) = -\frac{2\sqrt{3}L}{3} \left( C_a (\sin k_x + \sin k_y + \sin k_z) + \frac{1}{2R_m \omega} \right), \tag{D2}$$

$d_0(\mathbf{k}) = \frac{175}{12} LC_a$  for  $N = 3$ ,  $d_0(\mathbf{k}) = \frac{533}{24} LC_a$  for  $N = 4$ , and  $d_0(\mathbf{k}) = \frac{1771}{48} LC_a$  for  $N = 5$ . In Fig. 11, we present the frequency dispersion of the Weyl circuits. There are two Weyl points in the band structure for each case. Near the Weyl points, the dispersion is linear along with the  $k_z$  direction and  $N$ th order curve for  $k_x$  and  $k_y$ . The surface states in the (100) and (010) directions are shown in Fig. 11. The number of Fermi arcs is consistent with the topological charge of the Weyl points.

#### APPENDIX E: EXPERIMENTAL DETAILS OF THE WEYL CIRCUIT

The Weyl circuits for the experimental measurements are shown in Fig. 12. The parameters of the components are chosen as follows. Inductors  $L$  are 2.7  $\mu\text{H}$  with  $\pm 5\%$  tolerance. Capacitors  $C_a$  in the connection modules are 0.2 nF with  $\pm 5\%$  tolerance. Resistors  $R_m$  in modules  $U_0$  are 90.9  $\Omega$  with  $\pm 1\%$  tolerance, and resistors  $R_f$  are 2.8 k $\Omega$  with  $\pm 1\%$  tolerance. The operational amplifiers are AD8047. The voltages at each node, including the amplitude and phase, are probed by Rohde & Schwarz vector network analyzer ZNL6 5kHz-6GHz.

- [1] H. Weyl, Gravitation and the electron, *Proc. Natl. Acad. Sci. USA* **15**, 323 (1929).
- [2] X. Wan, A. M. Turner, A. Vishwanath, and S. Y. Savrasov, Topological semimetal and Fermi-arc surface states in the electronic structure of pyrochlore iridates, *Phys. Rev. B* **83**, 205101 (2011).
- [3] A. A. Burkov and L. Balents, Weyl semimetal in a topological insulator multilayer, *Phys. Rev. Lett.* **107**, 127205 (2011).
- [4] G. Xu, H. Weng, Z. Wang, X. Dai, and Z. Fang, Chern semimetal and the quantized anomalous Hall effect in  $\text{HgCr}_2\text{Se}_4$ , *Phys. Rev. Lett.* **107**, 186806 (2011).
- [5] L. Lu, L. Fu, J. D. Joannopoulos, and M. Soljačić, Weyl points and line nodes in gyroid photonic crystals, *Nat. Photonics* **7**, 294 (2013).
- [6] H. Weng, C. Fang, Z. Fang, B. A. Bernevig, and X. Dai, Weyl semimetal phase in noncentrosymmetric transition-metal monophosphides, *Phys. Rev. X* **5**, 011029 (2015).
- [7] S.-M. Huang, S.-Y. Xu, I. Belopolski, C.-C. Lee, G. Chang, B. Wang, N. Alidoust, G. Bian, M. Neupane, C. Zhang *et al.*, A Weyl fermion semimetal with surface Fermi arcs in the transition metal monpnictide TaAs class, *Nat. Commun.* **6**, 7373 (2015).
- [8] S.-Y. Xu, I. Belopolski, N. Alidoust, M. Neupane, G. Bian, C. Zhang, R. Sankar, G. Chang, Z. Yuan, C.-C. Lee *et al.*, Discovery of a Weyl fermion semimetal and topological Fermi arcs, *Science* **349**, 613 (2015).
- [9] B. Q. Lv, N. Xu, H. M. Weng, J. Z. Ma, P. Richard, X. C. Huang, L. X. Zhao, G. F. Chen, C. E. Matt, F. Bisti *et al.*, Observation of Weyl nodes in TaAs, *Nat. Phys.* **11**, 724 (2015).
- [10] A. A. Soluyanov, D. Gresch, Z. Wang, Q. Wu, M. Troyer, X. Dai, and B. A. Bernevig, Type-II Weyl semimetals, *Nature (London)* **527**, 495 (2015).
- [11] L. Huang, T. M. McCormick, M. Ochi, Z. Zhao, M.-T. Suzuki, R. Arita, Y. Wu, D. Mou, H. Cao, J. Yan *et al.*, Spectroscopic evidence for a type II Weyl semimetallic state in  $\text{MoTe}_2$ , *Nat. Mater.* **15**, 1155 (2016).
- [12] Q. Lin, M. Xiao, L. Yuan, and S. Fan, Photonic Weyl point in a two-dimensional resonator lattice with a synthetic frequency dimension, *Nat. Commun.* **7**, 13731 (2016).
- [13] Z. Wang, M. G. Vergniory, S. Kushwaha, M. Hirschberger, E. V. Chulkov, A. Ernst, N. P. Ong, R. J. Cava, and B. A. Bernevig, Time-reversal-breaking Weyl fermions in magnetic Heusler alloys, *Phys. Rev. Lett.* **117**, 236401 (2016).
- [14] M. Z. Hasan, S.-Y. Xu, I. Belopolski, and S.-M. Huang, Discovery of Weyl fermion semimetals and topological Fermi arc states, *Annu. Rev. Condens. Matter Phys.* **8**, 289 (2017).
- [15] N. P. Armitage, E. J. Mele, and A. Vishwanath, Weyl and Dirac semimetals in three-dimensional solids, *Rev. Mod. Phys.* **90**, 015001 (2018).
- [16] H. Nielsen and M. Ninomiya, Absence of neutrinos on a lattice (I). Proof by homotopy theory, *Nucl. Phys. B* **185**, 20 (1981).
- [17] H. Nielsen and M. Ninomiya, The Adler-Bell-Jackiw anomaly and Weyl fermions in a crystal, *Phys. Lett. B* **130**, 389 (1983).
- [18] S. A. Parameswaran, T. Grover, D. A. Abanin, D. A. Pesin, and A. Vishwanath, Probing the chiral anomaly with nonlocal transport in three-dimensional topological semimetals, *Phys. Rev. X* **4**, 031035 (2014).
- [19] S.-K. Jian, Y.-F. Jiang, and H. Yao, Emergent spacetime supersymmetry in 3D Weyl semimetals and 2D Dirac semimetals, *Phys. Rev. Lett.* **114**, 237001 (2015).
- [20] C. Chan and X.-J. Liu, Non-Abelian Majorana modes protected by an emergent second Chern number, *Phys. Rev. Lett.* **118**, 207002 (2017).
- [21] D. F. Liu, A. J. Liang, E. K. Liu, Q. N. Xu, Y. W. Li, C. Chen, D. Pei, W. J. Shi, S. K. Mo, P. Dudin *et al.*, Magnetic Weyl semimetal phase in a Kagomé crystal, *Science* **365**, 1282 (2019).
- [22] I. Belopolski, K. Manna, D. S. Sanchez, G. Chang, B. Ernst, J. Yin, S. S. Zhang, T. Cochran, N. Shumiya, H. Zheng *et al.*, Discovery of topological Weyl fermion lines and drum-head surface states in a room temperature magnet, *Science* **365**, 1278 (2019).
- [23] N. Morali, R. Batabyal, P. K. Nag, E. Liu, Q. Xu, Y. Sun, B. Yan, C. Felser, N. Avraham, and H. Beidenkopf, Fermi-arc diversity on surface terminations of the magnetic Weyl semimetal  $\text{Co}_3\text{Sn}_2\text{S}_2$ , *Science* **365**, 1286 (2019).
- [24] D. Wang, B. Yang, W. Gao, H. Jia, Q. Yang, X. Chen, M. Wei, C. Liu, M. Navarro-Cía, J. Han *et al.*, Photonic Weyl points due to broken time-reversal symmetry in magnetized semiconductor, *Nat. Phys.* **15**, 1150 (2019).
- [25] J.-Z. Ma, S. M. Nie, C. J. Yi, J. Jandke, T. Shang, M. Y. Yao, M. Naamneh, L. Q. Yan, Y. Sun, A. Chikina *et al.*, Spin fluctuation induced Weyl semimetal state in the paramagnetic phase of  $\text{EuCd}_2\text{As}_2$ , *Sci. Adv.* **5**, eaaw4718 (2019).
- [26] N. H. Jo, B. Kuthanazhi, Y. Wu, E. Timmons, T.-H. Kim, L. Zhou, L.-L. Wang, B. G. Ueland, A. Palasyuk, D. H. Ryan, R. J. McQueeney, K. Lee, B. Schrunck, A. A. Burkov, R. Prozorov, S. L. Bud'ko, A. Kaminski, and P. C. Canfield, Manipulating magnetism in the topological semimetal  $\text{EuCd}_2\text{As}_2$ , *Phys. Rev. B* **101**, 140402(R) (2020).
- [27] Z.-Y. Wang, X.-C. Cheng, B.-Z. Wang, J.-Y. Zhang, Y.-H. Lu, C.-R. Yi, S. Niu, Y. Deng, X.-J. Liu, S. Chen, and J.-W. Pan, Realization of an ideal Weyl semimetal band in a quantum gas with 3D spin-orbit coupling, *Science* **372**, 271 (2021).
- [28] B. Bradlyn, J. Cano, Z. Wang, M. Vergniory, C. Felser, R. J. Cava, and B. A. Bernevig, Beyond Dirac and Weyl fermions: unconventional quasiparticles in conventional crystals, *Science* **353**, aaf5037 (2016).
- [29] L. Lepori, I. C. Fulga, A. Trombettoni, and M. Burrello, Double Weyl points and Fermi arcs of topological semimetals in non-Abelian gauge potentials, *Phys. Rev. A* **94**, 053633 (2016).
- [30] B. J. Wieder, Y. Kim, A. M. Rappe, and C. L. Kane, Double Dirac semimetals in three dimensions, *Phys. Rev. Lett.* **116**, 186402 (2016).
- [31] S.-M. Huang, S.-Y. Xu, I. Belopolski, C.-C. Lee, G. Chang, T.-R. Chang, B. Wang, N. Alidoust, G. Bian *et al.*, New type of Weyl semimetal with quadratic double Weyl fermions, *Proc. Natl. Acad. Sci. U.S.A.* **113**, 1180 (2016).
- [32] Z. Zhu, G. W. Winkler, Q. S. Wu, J. Li, and A. A. Soluyanov, Triple point topological metals, *Phys. Rev. X* **6**, 031003 (2016).
- [33] P. Tang, Q. Zhou, and S.-C. Zhang, Multiple types of topological fermions in transition metal silicides, *Phys. Rev. Lett.* **119**, 206402 (2017).
- [34] G. Chang, S.-Y. Xu, B. J. Wieder, D. S. Sanchez, S.-M. Huang, I. Belopolski, T.-R. Chang, S. Zhang, A. Bansil, H. Lin, and M. Z. Hasan, Unconventional chiral fermions and large topological Fermi arcs in  $\text{RhSi}$ , *Phys. Rev. Lett.* **119**, 206401 (2017).

- [35] T. Zhang, Z. Song, A. Alexandradinata, H. Weng, C. Fang, L. Lu, and Z. Fang, Double-Weyl phonons in transition-metal monosilicides, *Phys. Rev. Lett.* **120**, 016401 (2018).
- [36] D. Takane, Z. Wang, S. Souma, K. Nakayama, T. Nakamura, H. Oinuma, Y. Nakata, H. Iwasawa, C. Cacho, T. Kim *et al.*, Observation of chiral fermions with a large topological charge and associated Fermi-arc surface states in CoSi, *Phys. Rev. Lett.* **122**, 076402 (2019).
- [37] N. Schröter, D. Pei, M. G. Vergniory, Y. Sun, K. Manna, F. De Juan, J. Krieger, V. Süß, M. Schmidt, P. Dudin *et al.*, Chiral topological semimetal with multifold band crossings and long Fermi arcs, *Nat. Phys.* **15**, 759 (2019).
- [38] Z. Rao, H. Li, T. Zhang, S. Tian, C. Li, B. Fu, C. Tang, L. Wang, Z. Li, W. Fan *et al.*, Observation of unconventional chiral fermions with long Fermi arcs in CoSi, *Nature (London)* **567**, 496 (2019).
- [39] N. B. M. Schröter, S. Stolz, K. Manna, F. de Juan, M. G. Vergniory, J. A. Krieger, D. Pei, T. Schmitt, P. Dudin, T. K. Kim *et al.*, Observation and control of maximal Chern numbers in a chiral topological semimetal, *Science* **369**, 179 (2020).
- [40] G. Chang, J.-X. Yin, T. Neupert, D. S. Sanchez, I. Belopolski, S. S. Zhang, T. A. Cochran, Z. Cheng, M.-C. Hsu, S.-M. Huang, B. Lian *et al.*, Unconventional photocurrents from surface Fermi arcs in topological chiral semimetals, *Phys. Rev. Lett.* **124**, 166404 (2020).
- [41] Y. Yang, Z. Gao, X. Feng, Y.-X. Huang, P. Zhou, S. A. Yang, Y. Chong, and B. Zhang, Ideal unconventional Weyl point in a chiral photonic metamaterial, *Phys. Rev. Lett.* **125**, 143001 (2020).
- [42] Q. Chen, F. Chen, Y. Pan, C. Cui, Q. Yan, L. Zhang, Z. Gao, S. A. Yang, Z.-M. Yu, H. Chen, B. Zhang, and Y. Yang, Discovery of a maximally charged Weyl point, *Nat. Commun.* **13**, 7359 (2022).
- [43] J. Ningyuan, C. Owens, A. Sommer, D. Schuster, and J. Simon, Time- and site-resolved dynamics in a topological circuit, *Phys. Rev. X* **5**, 021031 (2015).
- [44] V. V. Albert, L. I. Glazman, and L. Jiang, Topological properties of linear circuit lattices, *Phys. Rev. Lett.* **114**, 173902 (2015).
- [45] C. H. Lee, S. Imhof, C. Berger, F. Bayer, J. Brehm, L. W. Molenkamp, T. Kiessling, and R. Thomale, Topoelectrical circuits, *Commun. Phys.* **1**, 39 (2018).
- [46] K. Luo, R. Yu, and H. Weng, Topological nodal states in circuit lattice, *Research* **2018**, 6793752 (2018).
- [47] Y. Lu, N. Jia, L. Su, C. Owens, G. Juzeliunas, D. I. Schuster, and J. Simon, Probing the Berry curvature and Fermi arcs of a Weyl circuit, *Phys. Rev. B* **99**, 020302(R) (2019).
- [48] R. Li, B. Lv, H. Tao, J. Shi, Y. Chong, B. Zhang, and H. Chen, Ideal type-II Weyl points in topological circuits, *Natl. Sci. Rev.* **8**, nwa192 (2021).